JPE 19-1-30

https://doi.org/10.6113/JPE.2019.19.1.316
ISSN(Print): 1598-2092 / ISSN(Online): 2093-4718

Key Technologies of Supercapacitor Energy Storage System of IP Transmitter

Zhihui Zeng†, Xiaowei Wang*, Yanfang Wei*, Zhiguo Hu*, Yangxiao Yu*, and Zhigang Zhang**

†,*School of Electrical Engineering and Automation, Henan Polytechnic University, Jiaozuo, China
**College of Information Technology, Jiaozuo University, Jiaozuo, China

Abstract

A practical application of a supercapacitor energy storage system in a polarization instrument is proposed on the basis of the energy storage requirements of an induced polarization (IP) transmitter for geophysical exploration. We focused on the energy storage system of a supercapacitor, the topology of the power converter, and the system control strategy as key technologies, and we performed theoretical research and experimental tests on the system and developed an experimental platform. The experiments validated the theoretical research on the key technologies of the supercapacitor energy storage system and demonstrated the effectiveness of the innovation. Results showed that the storage system is efficient and satisfies the energy storage needs of the IP transmitter.

Key words: Efficient, Key technology, Polarization apparatus, Storage system, Supercapacitor

I. INTRODUCTION

The time-domain induced polarization (IP) method is a traditional geophysical prospecting technique that is widely used in metal detection. The IP instrument used for metal exploration comprises a transmitter, which plays an important role, and a receiver. The reliability and stability of the transmitted signal directly determine the performance of the instrument. The stronger the electric field produced by the transmitter, the higher the accuracy, reliability, and signal-to-noise ratio of the polarizability signal. In a time-domain IP instrument, the transmitter (IP transmitter) technology operates in a working cycle during only half of which the system operates with a load. Consequently, the speed of the field transmitter and the power supply voltage are unstable, and electric energy is wasted during the no-load period.

In this context, a supercapacitor energy storage system that stores the energy produced by generators when the transmitter does not operate and releases the stored energy when the transmitter operates is proposed for stabilizing generators' power supply; saving energy; and reducing generators' rated power, volume, and weight. Given that this type of equipment is commonly used in field operations, the equipment requirements are stringent, and supercapacitors' energy storage systems are designed for high efficiency, high reliability, high power density, high stability, and fast response.

The efficiency, weight, volume, and cost of present supercapacitor energy storage systems determine system development and application. A large-capacity and high-density electric energy storage method and advanced control technology will considerably reduce the volume and weight of systems and reduce the cost of energy storage. With a solution to the problem of energy conversion and guaranteed rapid and efficient conversion, the performance and efficiency of the energy storage systems are substantially improved. By improving the energy storage method and ensuring fast and efficient charging and discharging cycles, the proposed energy storage system for IP transmitter systems becomes suitable for practical applications.

In this study, we propose a supercapacitor energy storage system for practical applications of a polarization instrument (IP transmitter). We establish a simplified model of the supercapacitor and design an improved cascaded bi-directional buck/boost-LLC DC/DC converter topological structure that considerably reduces system loss and improves the conversion efficiency of the power converter. We propose a sliding mode

Manuscript received Feb. 8, 2018; accepted Sep. 28, 2018
Recommended for publication by Associate Editor Se-Kyo Chung.
†Corresponding Author: zzhh@hpu.edu.cn
Tel: +86-186-0391-7375, Henan Polytechnic University
*School of Electrical Eng. and Autom., Henan Polytechnic Univ., China
**College of Information Technology, Jiaozuo University, China

© 2019 KIPE

control strategy for the supercapacitor storage system that is based on the cascaded bi-directional buck/boost-LLC DC/DC converters, which ensure that the DC energy storage unit of the supercapacitor is safe and stable and operates quickly in a large working range. A prototype of the supercapacitor energy storage system with a power of 10 kW in the IP transmitter is developed, and related experiments are conducted.

II. System Topological Analysis

On the basis of the technical requirements of the energy storage system of an IP transmitter, the power converter of the supercapacitor energy storage system must meet the requirements of the precise regulations for output voltage, variations in the terminal voltage range after charging and discharging of the supercapacitor group, and high efficiency and high-power density during bi-directional flow. For this purpose, we select the bi-directional buck/boost-LLC DC/DC converter with a low-voltage side boost + LLC topology structure as the power converter of the supercapacitor energy storage system. The main circuit topology of the system is shown in Fig. 1.

The supercapacitor group represents the energy storage unit of the system, and a simplified equivalent model is used for completing the charging and discharging functions. A bi-directional power converter, that is, cascade bi-directional buck/boost-LLC DC/DC converter, is connected to the supercapacitor group. The buck/boost DC/DC converter is used for the non-isolated level of the converter, and the bi-directional full-bridge LLC DC/DC converter is used for the isolated level of the converter. The non-isolated stage converter has a high working efficiency and few switching devices and performs voltage regulation; the isolated stage converter operates at an optimal state of efficiency under the voltage regulation of the former stage converter. The low-voltage side of the buck/boost level converter in the system is part of the supercapacitor energy storage unit. The high-voltage side is connected to the low-voltage side of the LLC level converter, which provides a stable DC bus voltage for the LLC level converter. With the combination of the topologies of the bi-directional full-bridge DC/DC converter and the LLC resonant converter, a new type of bi-directional full-bridge LLC DC/DC converter is developed; its low- and high-voltage sides are connected to the output terminal of the buck/boost level converter and an external load, respectively. Soft switching is achieved for the full load range of the system's power converter, which reduces the circuit switching loss and improves the operating efficiency and the power density of the converter. The power converter topology (Fig. 1) shows that the main losses of the low-voltage side cascade boost+LLC converter are the insulated-gate bipolar transistor (IGBT) losses of the two-stage converter, the energy storage inductance, the resonant inductance, and the transformer.

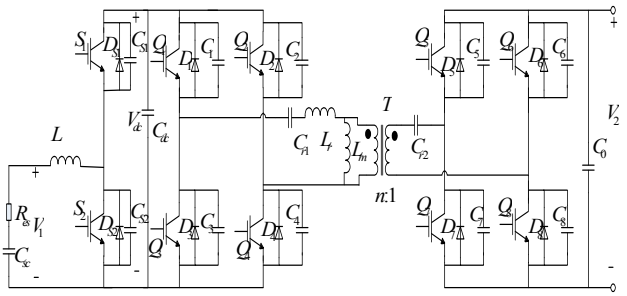

Fig. 1. Main circuit topology of the supercapacitor energy storage system.

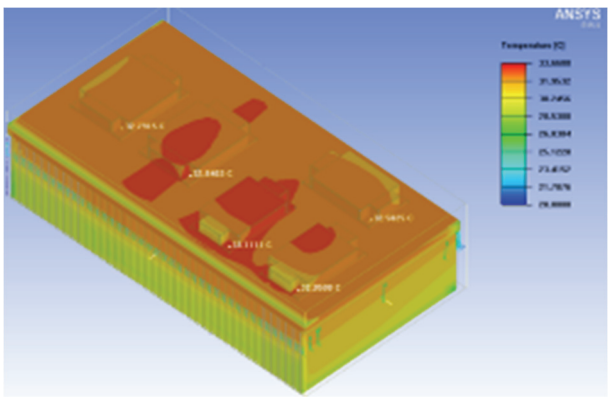

Fig. 2. Simulation model.

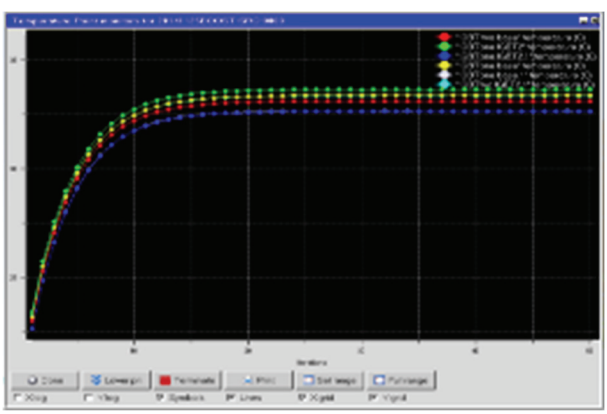

Fig. 3. Temperature curve of the main switching tube.

A thermal simulation of the main components of the cascaded boost+LLC converter used in the low-voltage side of the system is conducted for obtaining the loss of the main switching devices (IGBT) of the converter. The software SolidWorks is used for simulating the structure of the IGBT device in the system topology, and the thermal simulation model of the device is shown in Fig. 2. The finite element analysis software ANSYS Icepak is used for simulating the main switching devices, and the results showing the temperature increases are depicted in Fig. 3. The thermal simulation results show that the main switching temperature is near 33 °C.

The theoretical calculations show that the efficiency of the low-voltage side cascaded boost converter is 97.02% at a power level of 10 kW, and the thermal simulation results show that the main switching temperature is near 33 °C and is in a state of low heat loss. The topological structure does not only satisfy the system's energy storage requirements but also effectively improves the energy efficiency of the storage system. Therefore, we use the cascaded bi-directional buck/boost-LLC DC/DC converter topology structure in this study for the supercapacitor energy storage system.

III. System Control Strategy

A sliding mode control strategy is proposed for controlling the bi-directional DC/DC power converter of the energy storage system, achieving flexibility during energy charging and discharging, improving the soft characteristics of the terminal voltage of the supercapacitor, and ensuring that the DC energy storage unit of the supercapacitor is safe and stable and operates quickly in a wide working range.

The sliding mode control strategy presented in this paper is applied to the design of the sliding mode trajectory in the dynamic process of the switching converter for the best dynamic characteristics to be determined. Thus, a state space average linearized small signal equivalent model does not need to be established. In addition, the disturbance mode of the external large-signal disturbance is completely self-adaptive and robust. In this study, a sliding mode controller is designed for the bi-directional power flow.

A. Analysis of the System Control Strategy of the Boost Working Mode

The objectives are to maintain the stability of the bus voltage and ensure the lowest voltage of the supercapacitor energy storage unit when the power of the supercapacitor energy system is in a forward flow mode, the non-isolated buck/boost DC/DC converter operates in the boost mode, and the supercapacitor is in the discharge state, as shown in Fig. 1. When the boost converter operates in a continuous conduction mode, the duty ratio to output voltage transfer function has a right-half-plane zero (RHPZ), which usually leads to the dynamic hysteresis of the control system, especially when the voltage mode control is used. The existence of RHPZ increases the complexity of the design of the controller and substantially limits the broadband of the voltage mode controller compensation network. Therefore, for achieving a fast, dynamic response for this type of converter system, the current-mode control is usually used; however, it is not suitable for a converter in a very-large-scale operating state because of the disadvantages of excessive overshoot and long adjustment time. For converters in boost working state, a sliding mode controller is designed with use of the fixed-frequency sliding mode current control proposed in this study. The controller uses the output voltage error and the inductor current error as control state variables and the output voltage error to adjust the output voltage accurately. Meanwhile, the inductance current is near the reference value that is based on the error of the inductor current. The sliding mode controller is implemented in a fixed-frequency sliding mode control, which results in a faster dynamic response for the constant-frequency sliding mode current control of the boost controller than the conventional current-mode and maintains stability under a wide range of operating conditions. With the system working in a wide range of changes, the adjustment time and the contrast between the voltage overshoot and the conventional current-mode are very small, which effectively solves the problems that occur in the conventional current-mode control.

1) System Modeling of Boost Working Mode

The system produces an instant reference inductor current i_{ref} using the same amplified output voltage error as that of the conventional pulse-width modulation (PWM) current-mode control.

$$i_{ref} = K(V_{ref} - \beta v_{dc}), \tag{1}$$

where V_{ref} and v_{dc} are the output voltage reference and instantaneous values, respectively; β is the feedback network ratio; and K is the voltage error amplification gain.

For the boost converter with a sliding mode current control, control variable x is expressed as

$$x = \begin{bmatrix} x_1 \\ x_2 \\ x_3 \end{bmatrix} = \begin{bmatrix} i_{ref} - i_L \\ V_{ref} - \beta v_{dc} \\ \int [x_1 + x_2]dt \end{bmatrix} = \begin{bmatrix} i_{ref} - i_L \\ V_{ref} - \beta v_{dc} \\ \int (i_{ref} - i_L)dt + \int (V_{ref} - \beta v_{dc})dt \end{bmatrix}, \tag{2}$$

where x_1, x_2, x_3 are the current error, voltage error, and the error integral of the current and voltage, respectively.

The state equation of the small-signal model of the converter working in boost mode is

$$\begin{cases} L\dfrac{di_L(t)}{dt} = v_1 - d'v_{dc} \\ C_{dc}\dfrac{dv_{dc}}{dt} = d'i_L - \dfrac{v_{dc}}{r_L} \end{cases}, \tag{3}$$

where $d' = 1 - d$ and d is the drive signal duty cycle of the switch tube (S_2).

According to the equivalent control method, if we regard the converter's output terminal load as a resistive load, then the dynamic model of the system is described as

$$\dot{x}=\begin{bmatrix}\dot{x}_1\\ \dot{x}_2\\ \dot{x}_3\end{bmatrix}=\begin{bmatrix}\dfrac{-\beta K}{C_{dc}}i_{dc}-\dfrac{v_1-(1-u_{eq})v_{dc}}{L}\\ \dfrac{-\beta}{C_{dc}}i_{dc}\\ (K+1)[V_{ref}-\beta v_{dc}]-i_L\end{bmatrix}. \quad (4)$$

By substitution of the expression $i_{dc}=i_L-i_r$ and Eqs. (2) and (3) into Eq. (4), we obtain

$$\dot{x}=\begin{bmatrix}\dot{x}_1\\ \dot{x}_2\\ \dot{x}_3\end{bmatrix}=\begin{bmatrix}\dfrac{\beta K}{C_{dc}}x_1-\dfrac{\beta K^2}{C_{dc}}x_2-\dfrac{v_{dc}}{L}u_{eq}+(\dfrac{\beta K}{C_{dc}r_L}+\dfrac{1}{L})v_{dc}-\dfrac{v_1}{L}\\ \dfrac{\beta}{C_{dc}}x_1-\dfrac{\beta K}{C_{dc}}x_2+\dfrac{\beta}{C_{dc}r_L}v_{dc}\\ x_1+x_2-\dfrac{1}{r_L}v_{dc}\end{bmatrix}. \quad (5)$$

Therefore, the state-space equation of the boost converter can be obtained as

$$\dot{x}=Ax+Bv+D, \quad (6)$$

$$A=\begin{bmatrix}\dfrac{\beta K}{C_{dc}} & -\dfrac{\beta K^2}{C_{dc}} & 0\\ \dfrac{\beta}{C_{dc}} & -\dfrac{\beta K}{C_{dc}} & 0\\ 1 & 1 & 0\end{bmatrix},B=\begin{bmatrix}-\dfrac{v_{dc}}{L}\\ 0\\ 0\end{bmatrix},D=\begin{bmatrix}(\dfrac{\beta K}{C_{dc}r_L}+\dfrac{1}{L})v_{dc}-\dfrac{v_1}{L}\\ \dfrac{\beta}{C_{dc}r_L}v_{dc}\\ -\dfrac{1}{r_L}v_{dc}\end{bmatrix},x=\begin{bmatrix}x_1\\ x_2\\ x_3\end{bmatrix}.$$

2) Design of the Sliding Mode Controller of the Boost Working Mode

The sliding mode control law of the controller is expressed by the switching function

$$u=\begin{cases}1 & \text{when } s>0\\ 0 & \text{when } s<0\end{cases}. \quad (7)$$

S is the instant state trajectory and expressed as

$$s=\alpha_1x_1+\alpha_2x_2+\alpha_3x_3=J^Tx. \quad (8)$$

$J^T=[\alpha_1,\alpha_2,\alpha_3],\alpha_1,\alpha_2,\alpha_3$ is the sliding coefficient. To ensure the existence of the sliding mode, the following conditions are required:

$$\lim_{s\to 0}s\cdot\dot{s}<0. \quad (9)$$

Using Eq. (8) in Eq. (9), we obtain

$$\begin{cases}\dot{s}_{s\to 0^+}=J^TAx+J^TBv_{s\to 0^+}+J^TD<0\\ \dot{s}_{s\to 0^-}=J^TAx+J^TBv_{s\to 0^-}+J^TD>0\end{cases}. \quad (10)$$

Make $\dot{S}=J^TAx+J^TBu_{eq}+J^TD=0$ to obtain the equivalent control function

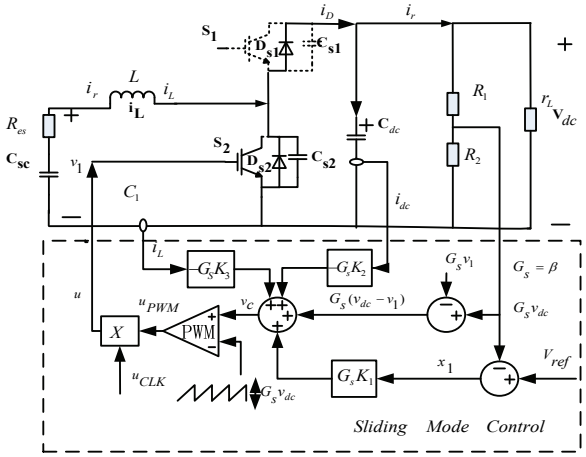

Fig. 4. Schematic of the sliding mode current controller of the boost mode.

$$u_{eq}=1-\frac{K_2}{v_{dc}}i_{dc}-\frac{v_1}{v_{dc}}+\frac{K_1}{v_{dc}}(V_{ref}-\beta v_{dc})-\frac{K_3}{v_{dc}}i_L, \quad (11)$$

$K_1=L\dfrac{\alpha_3}{\alpha_1}(K+1),K_2=\dfrac{\beta L}{C_{dc}}(K+\dfrac{\alpha_2}{\alpha_1}),K_3=L\dfrac{\alpha_3}{\alpha_1}$. Make $u_{eq}=d$ to obtain the expression of the control signal and the slope signal.

$$\begin{cases}v_c=G_sK_1(V_{ref}-\beta v_{dc})-G_sK_2i_{dc}-G_sK_3i_L+G_s[v_{dc}-v_1]\\ \hat{}\\ v_{ramp}=G_sv_{dc}\end{cases} \quad (12)$$

G_s is designed using Eq. (11), where $0<G_s<1$, for reducing the value of the equation and meeting the voltage level requirements in the circuit implementation. To ensure that the duty radio produced by the controller is always less than 1, the control signal modulated by the system and the pulse signal generated by the pulse generator are usually multiplied. The control principle diagram of the converter when $G_s=\beta$ is shown in Fig. 4.

B. Analysis of the System Control Strategy of the Buck Working Mode

When the system power flows in the opposite direction of the supercapacitor energy storage system, the supercapacitors are in the charge state, and the non-isolated buck/boost DC/DC converter operates in buck mode. The control targets in this mode are such that the voltage at both ends of the supercapacitor reaches a predetermined value and the terminal voltage remains stable. In this study, the PWM sliding mode voltage control method is used for designing the sliding mode controller of the buck state of the converter. The controller uses a proportion-integration-differentiation (PID) synovial voltage control for the sliding mode controller. During the controller's design, the voltage error integral term

is added, which effectively reduces the steady-state error of the actual sliding mode control; the equivalent control method is used to control the control signal u_{eq} in the sliding mode control and the duty radio signal "d" of the PWM controller, thereby achieving fixed-frequency sliding mode control.

1) System Modeling of the Buck Working Mode

For the PID sliding mode voltage controller (SMVC) buck converter, control variable x is expressed as

$$x=\begin{bmatrix}x_1\\x_2\\x_3\end{bmatrix}=\begin{bmatrix}V_{ref}-\beta v_1\\ \dfrac{d(V_{ref}-\beta v_1)}{dt}\\ \int(V_{ref}-\beta v_1)dt\end{bmatrix}, \tag{13}$$

where x_1, x_2, x_3 are the voltage error, voltage dynamic error, and voltage error integral, respectively. The state equation of the buck converter for the small-signal modeling is

$$\begin{cases}L\dfrac{di_L(t)}{dt}=dv_{dc}-v_1\\ C_1\dfrac{dv_1}{dt}=i_L-\dfrac{v_0}{r_L}\end{cases}. \tag{14}$$

According to the equivalent control method, we set $u_{eq}=d$; therefore, the equivalent model of the supercapacitor is equivalent to a resistive load. The expression of control variable x can be described by Eq. (15).

$$x=\begin{bmatrix}x_1\\x_2\\x_3\end{bmatrix}=\begin{bmatrix}x_1=V_{ref}-\beta v_1\\ x_2=\dfrac{\beta v_1}{r_L C}+\int\dfrac{\beta(v_1-u_{eq}v_{dc})}{LC}\\ x_3=\int x_1 dt\end{bmatrix} \tag{15}$$

Therefore, the state-space equation of the buck converter is

$$\dot{x}=Ax+Bv+D, \tag{16}$$

$$A=\begin{bmatrix}0&1&0\\0&-\dfrac{1}{r_L C}&0\\1&0&0\end{bmatrix}, B=\begin{bmatrix}0\\-\dfrac{\beta v_{dc}}{LC}\\0\end{bmatrix}, D=\begin{bmatrix}0\\ \dfrac{\beta v_1}{LC}\\0\end{bmatrix}, x=\begin{bmatrix}x_1\\x_2\\x_3\end{bmatrix}.$$

2) Design of the Sliding Mode Controller of the Buck Working Mode

By substituting the rate control function in Eq. (8) into Eq. (10), we obtain the following:

a): $s\to 0^{+}, \dot{s}<0$

$$-\alpha_1\frac{\beta i_{C1}}{C_1}+\alpha_2\frac{\beta i_{C1}}{r_L C_1{}^2}+\alpha_3(V_{ref}-\beta v_1)-\alpha_2\frac{\beta v_{dc}}{LC_1}+\alpha_2\frac{\beta v_1}{LC_1}<0, \tag{17}$$

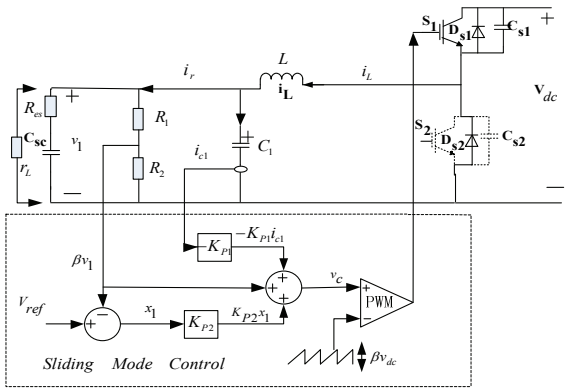

Fig. 5. Schematic of the PWM of the PID SMVC buck converter.

b): $s\to 0^{-}, \dot{s}>0$

$$-\alpha_1\frac{\beta i_{C1}}{C_1}+\alpha_2\frac{\beta i_{C1}}{r_L C_1{}^2}+\alpha_3(V_{ref}-\beta v_1)+\alpha_2\frac{\beta v_1}{LC_1}>0. \tag{18}$$

By simplifying Eqs. (17) and (18), we obtain

$$0<-\beta L(\frac{\alpha_1}{\alpha_2}-\frac{1}{r_L C_1})i_{C1}+LC_1\frac{\alpha_3}{\alpha_2}(V_{ref}-\beta v_1)+\beta v_1<\beta v_{dc}. \tag{19}$$

According to the invariance condition of the sliding mode control, the equivalent control signal u_{eq} is set to $\dot{s}=0$, which results in $\dot{s}=J^T Ax+J^T Bu_{eq}+J^T D=0$.

The equivalent control function is

$$u_{eq}=-[J^T B]^{-1}J^T[Ax+D]$$

$$=-\frac{\beta L}{\beta v_{dc}}(\frac{\alpha_1}{\alpha_2}-\frac{1}{r_L C_1})i_{C1}+LC_1\frac{\alpha_3}{\alpha_2\beta v_{dc}}(V_{ref}-\beta v_1)+\frac{v_1}{v_{dc}}. \tag{20}$$

We require u_{eq} to meet $0<u_{eq}<1$, according to Eq. (20).

$$0<u_{eq}=-\frac{\beta L}{\beta v_{dc}}(\frac{\alpha_1}{\alpha_2}-\frac{1}{r_L C_1})i_{C1}+LC_1\frac{\alpha_3}{\alpha_2\beta v_{dc}}(V_{ref}-\beta v_1)+\frac{v_1}{v_{dc}}<1, \tag{21}$$

$$0<u^*{}_{eq}=-\beta L(\frac{\alpha_1}{\alpha_2}-\frac{1}{r_L C_1})i_{C1}+LC_1\frac{\alpha_3}{\alpha_2}(V_{ref}-\beta v_1)+\beta v_1<\beta v_{dc}. \tag{22}$$

By transforming Eq. (33) to duty cycle "d", $0<d=\dfrac{vc}{\hat{v}ramp}<1$, we obtain

$$v_c=u^*{}_{eq}=-\beta L(\frac{\alpha_1}{\alpha_2}-\frac{1}{r_L C_1})i_{C1}+LC_1\frac{\alpha_3}{\alpha_2}(V_{ref}-\beta v_1)+\beta v_1, \tag{23}$$

$$\hat{v}ramp=\beta v_{dc}. \tag{24}$$

According to Eqs. (23) and (24), the basic design of the PWM sliding mode controller can be achieved. Set $K_{P1}=\beta L(\frac{\alpha_1}{\alpha_2}-\frac{1}{r_L C_1}), K_{P2}=LC_1\frac{\alpha_3}{\alpha_2}$ and Eq. (24) to

$$v_c=-K_{P1}i_{C1}+K_{P2}(V_{ref}-\beta v_1)+\beta v_1. \tag{25}$$

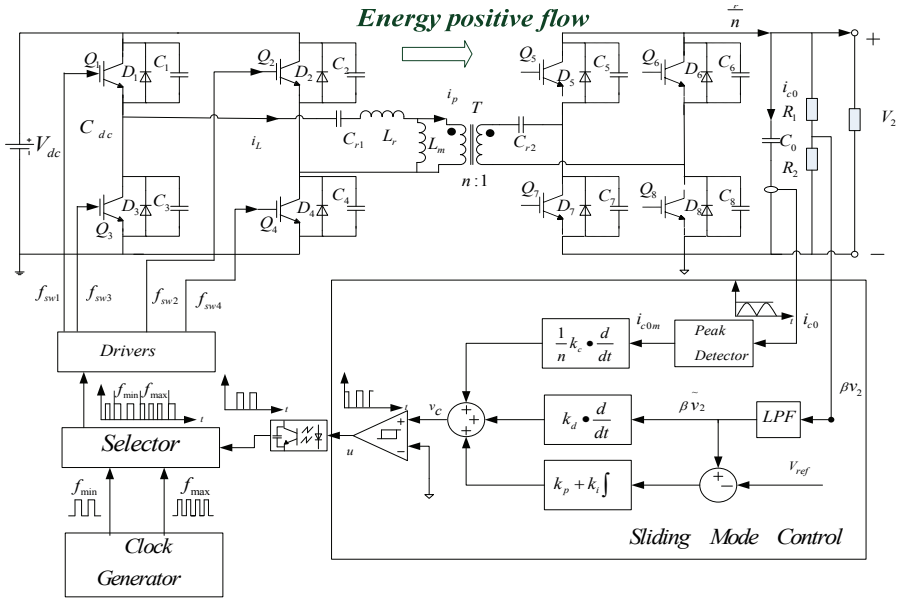

Fig. 6. Schematic of the sliding mode current controller for the LLC converter.

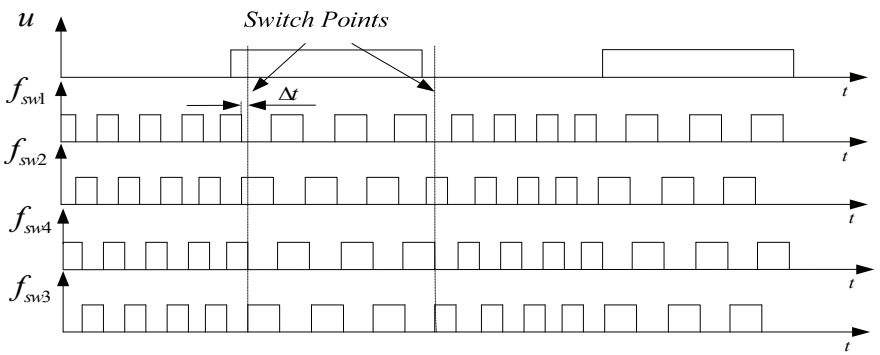

Fig. 7. Schematic of ZCS.

Equation (25) is the control signal of the sliding mode controller; therefore, we can obtain the sliding mode controller of the buck converter. The control schematic is shown in Fig. 5.

C. Analysis of the System Control Strategy of the Full-Bridge Bi-Directional LLC DC/DC Converter

In this study, we analyze the full-bridge bi-directional LLC DC/DC converter sliding mode controller and propose a discrete pulse frequency modulation mode. The converter only works for the discrete switching frequency points $f_{\min}$ and $f_{\max}$. The sliding mode control signal that corresponds to the two specific discrete switching frequencies, its frequency, and its sliding mode control signal is defined as follows:

$$f = f_{\max} + (f_{\min} - f_{\max})u \,, \tag{26}$$

$$u = \begin{cases} 0 \\ 1 \end{cases} . \tag{27}$$

A block diagram of the full-bridge bi-directional LLC DC/DC converter operating in the forward direction with the sliding mode control system is shown in Fig. 6. The control system uses the converter output voltage and the output filter capacitor current feedback as the system state variables. A sliding mode control signal u is generated by the hysteresis comparator and subsequently passes through optical coupling to the primary drive signal selector, and we select the system's fixed operating frequency, $f_{\min}$ or $f_{\max}$, for the converter to operate at a specific discrete switching frequency. Finally, the drive circuit of the full-bridge switch device is driven by the signal driving circuit, which achieves the closed-loop control of the system. The system performs sliding mode chattering suppression against the converter in a variable-frequency operating condition in hysteresis mode, whereas optical coupling isolation is used for the signal transmission of the sliding mode control to ensure superior dynamic performance of the system. To guarantee the effective and stable operation of the circuit when the frequency is switched using two specific switches, the

converter must satisfy the condition of "zero-crossing switching" (ZCS), which means that the converter can be switched between the two specific frequencies only after a complete switching period. The implementation of the switching circuit is designed in the rear. A schematic of ZCS is shown in Fig. 7, where Δt represents the dead-time setting by the system. ZCS guarantees the stable operation of the system, while control delay is added to the system.

1) System Modeling of the Full-Bridge Bi-Directional LLC DC/DC Converter

The extended description function is used to model the full-bridge bi-directional LLC DC/DC converter. First, the resonant converter is modularized, and the converter is divided into four modules, including the switching network, the resonant tank, the rectifying network, and the filter network. Second, the nonlinear state equation of the entire circuit of the converter is derived, and the extended description function is used to deal with the nonlinear process. Third, the harmonic balance method is used to model the large signal.

The following assumptions are made.

a) All the switches in the circuit are ideal, and any parasitic parameter is ignored.
b) The passive devices are regarded as linear time-invariant components, and the corresponding losses are expressed by the equivalent resistance.
c) The filter corner frequency is considerably smaller than the switching frequency.
d) The disturbances during the analysis process are small-signal perturbations.
e) The usual assumption is that the switching frequency is near the resonant frequency.

According to the above assumptions, the secondary power converter means that the full-bridge bi-directional LLC DC/DC converter (shown in Fig. 1) is equivalent to the equivalent circuit diagram of the full-bridge bi-directional LLC resonant converter shown in Fig. 8.

The input voltage (v_{in}) of the resonant tank is the output voltage of the switching network in Fig. 1. The voltage waveform is a square wave, its duty cycle is d, its amplitude is $\frac{4V_{dc}}{\pi}$, and its frequency is the same as the switching frequency. In Fig. 8, R_r, n represent the inductance, the equivalent resistance, and the transformation ratio of the transformer. The output variables are expressed by V_2 in the general system chart.

We select the resonant inductor current (I_1), the transformer excitation inductance current (I_2), the resonant capacitor voltage (V_1), and the output filter capacitor voltage (V_2) as the state variables. According to the equivalent circuit shown in Fig. 8, the system's nonlinear differential equations of the state are

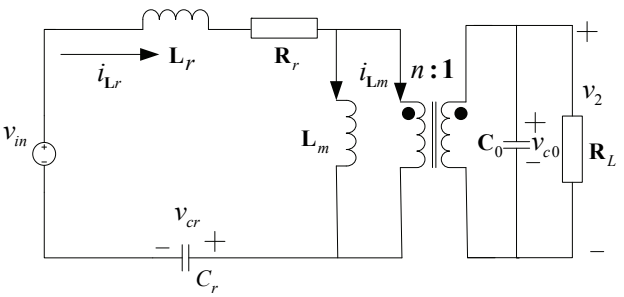

Fig. 8. Equivalent circuit diagram in forward-working mode.

$$\begin{cases} v_{in} = L_r \dfrac{di_{Lr}}{dt} + v_{cr} + L_m \dfrac{di_{Lm}}{dt} + R_r i_{Lr} \\ L_m \dfrac{di_{Lm}}{dt} = n\,\mathrm{sgn}(i_{Lr} - i_{Lm}) v_2 \\ i_{Lr} = C_r \dfrac{dv_{cr}}{dt} \\ \dfrac{v_{c0}}{R_L} + C_0 \dfrac{dv_{c0}}{dt} = nabs(i_{Lr} - i_{Lm}) \end{cases}, \quad (28)$$

where $v_{in}, \mathrm{sgn}(i_{Lr} - i_{Lm}), abs(i_{Lr} - i_{Lm})$ is a nonlinear variable where $\mathrm{sgn}(i_{Lr} - i_{Lm})$ is a symbolic function and $i_{Lr} - i_{Lm}$ is the current that flows through the primary side of the transformer. When $i_{Lr} - i_{Lm} > 0$, then $\mathrm{sgn}(i_{Lr} - i_{Lm})$ =1, indicating that the voltage at both ends of i_{Lm} is the same as the reference direction; when $i_{Lr} - i_{Lm} < 0$, then $\mathrm{sgn}(i_{Lr} - i_{Lm}) = -1$, and the voltage of i_{Lm} at this time is opposite to the reference direction. $abs(i_{Lr} - i_{Lm})$ is a representation of the absolute value of $i_{Lr} - i_{Lm}$.

We perform linear processing of Eq. (28) through the extended description function and obtain the large-signal model of the system on the basis of the principle of harmonic balance.

$$\begin{cases} \dfrac{di_{Lrm}}{dt} = \dfrac{1}{L_r}\left(\dfrac{4}{\pi} v_{dc}\cos\alpha - v_{crm}\cos(\alpha-\gamma) - \dfrac{4}{\pi} m v_{c0}\cos(\alpha-\beta)\right) \\ \dfrac{di_{pm}}{dt} = \dfrac{1}{L_{eq}}\left(\dfrac{L_{eq}}{L_r}\dfrac{4}{\pi} v_{dc}\cos\beta - \dfrac{L_{eq}}{L_r} v_{crm}\cos(\beta-\gamma) - \dfrac{4}{\pi} m v_{c0}\right) \\ \dfrac{dv_{crm}}{dt} = \dfrac{1}{C_r} i_{Lrm}\cos(\alpha-\gamma) \\ \dfrac{d\alpha}{dt} = \dfrac{1}{i_{Lrm} L_r}\left(\dfrac{4}{\pi} v_{dc}\sin\alpha + v_{crm}\sin(\alpha-\gamma) + \dfrac{4}{\pi} m v_{c0}\sin(\alpha-\beta)\right) - \omega \\ \dfrac{d\beta}{dt} = \dfrac{1}{i_{pm} L_{eq}}\left(-\dfrac{L_{eq}}{L_r}\dfrac{4}{\pi} v_{dc}\sin\beta + \dfrac{L_{eq}}{L_r} v_{crm}\sin(\beta-\gamma)\right) - \omega \\ \dfrac{d\gamma}{dt} = \dfrac{1}{v_{crm} C_r} i_{Lrm}\sin(\alpha-\gamma) - \omega \\ \dfrac{dv_2}{dt} = \dfrac{1}{C_0}\left(\dfrac{2n}{\pi} i_{pm} - \dfrac{v_2}{R_L}\right) \end{cases}, \quad (29)$$

where $L_{eq} = \dfrac{L_r L_m}{L_r + L_m}$,

$$\begin{cases} \sin\alpha=\dfrac{i_{Lrc}}{\sqrt{(i_{Lrs})^2+(i_{Lrc})^2}},\cos\alpha=\dfrac{i_{Lrs}}{\sqrt{(i_{Lrs})^2+(i_{Lrc})^2}} \\ \sin\beta=\dfrac{i_{Lrc}-i_{Lmc}}{\sqrt{(i_{Lrs}-i_{Lms})^2+(i_{Lrc}-i_{Lmc})^2}},\cos\beta=\dfrac{i_{Lrs}-i_{Lms}}{\sqrt{(i_{Lrs}-i_{Lms})^2+(i_{Lrc}-i_{Lmc})^2}} \\ \sin\gamma=\dfrac{v_{crc}}{\sqrt{(v_{crs})^2+(v_{crc})^2}},\cos\gamma=\dfrac{v_{crs}}{\sqrt{(v_{crs})^2+(v_{crc})^2}} \\ i_{pm}=\sqrt{(i_{Lrs}-i_{Lms})^2+(i_{Lrc}-i_{Lmc})^2},i_{Lrm}=\sqrt{(i_{Lrs})^2+(i_{Lrc})^2} \\ i_{Lmm}=\sqrt{(i_{Lms})^2+(i_{Lmc})^2} \\ v_{crm}=\sqrt{(v_{crs})^2+(v_{crc})^2} \end{cases}.$$

2) Design of the Sliding Mode Controller of the Full-Bridge Bi-Directional LLC DC/DC Converter

With use of the extended description for the signal modeling of the LLC converter and an input/output feedback linearization method, the complex nonlinear system analysis problem is transformed into a traditional linear system design problem. The input/output feedback linearization method is combined with the variable structure control with the sliding mode, the sliding mode control equations are obtained, and the partial linearization subsystem, including the variable, is derived using Eq. (29).

For the model of the single-input single-output (SISO) nonlinear system described in Eq. (29), we first determine the relative degree of the system, which is

$$\begin{cases} \dfrac{\partial}{\partial u}\left(\dfrac{d^{\lambda}v_2}{dt^{\lambda}}\right)=0 & \lambda=1,2 \\ \dfrac{\partial}{\partial u}\left(\dfrac{d^{\lambda}v_2}{dt^{\lambda}}\right)\neq 0 & \lambda=3 \end{cases}. \tag{30}$$

According to Eq. (30), the relative degree of the system is 3; on the basis of the input/output feedback linearization method, the response characteristic of the output voltage is assumed to be

$$b_3\beta\frac{d^3v_2}{dt^3}+b_2\beta\frac{d^2v_2}{dt^2}+b_1\frac{d(\beta v_2-V_{ref})}{dt}+b_0(\beta v_2-V_{ref})=0, \tag{31}$$

where βv_2-V_{ref} reflects the system's steady-state information, and the output response coefficients $b_3\beta$, $b_2\beta$, b_1, and b_0 can be obtained.

Eq. (29) can be transformed as follows:

$$C_0\frac{d^3v_2}{dt^3}+\frac{1}{R_L}\frac{d^2v_2}{dt^2}-n\frac{2}{\pi}\frac{d^2i_{pm}}{dt^2}=0. \tag{32}$$

We set $a_3=L_{eq}C_0, a_2=\dfrac{L_{eq}}{R_L}, a_1=0, a_0=n\dfrac{2}{\pi}L_{eq}$ and then use Eq. (32) to derive

$$a_3\frac{d^3v_2}{dt^3}+a_2\frac{d^2v_2}{dt^2}+a_1\frac{dv_2}{dt}+a_0\frac{d^2i_{pm}}{dt^2}=0. \tag{33}$$

According to Eqs. (31) and (33),

$$(b_3\beta-a_3)\frac{d^3v_2}{dt^3}+(b_2\beta-a_2)\frac{d^2v_2}{dt^2}+b_1\frac{d(\beta v_2-V_{ref})}{dt}+b_0(\beta v_2-V_{ref})+a_0\frac{d^2i_{pm}}{dt^2}=0. \tag{34}$$

A sliding mode control surface is established for ensuring appropriate output voltage response and the invariance condition $\dot{s}=0$ of the sliding mode region.

$$\begin{aligned} \dot{s}=&(b_3\beta-a_3)\frac{d^3v_2}{dt^3}+(b_2\beta-a_2)\frac{d^2v_2}{dt^2}+b_1\frac{d(\beta v_2-V_{ref})}{dt} \\ &+b_0(\beta v_2-V_{ref})+a_0\frac{d^2i_{pm}}{dt^2}=0 \end{aligned} \tag{35}$$

Then, the equation of the sliding mode control surface is

$$\begin{aligned} s=&(b_3\beta-a_3)\frac{d^2v_2}{dt^2}+(b_2\beta-a_2)\frac{dv_2}{dt}+b_1\beta v_2 \\ &-V_{ref}+b_0\int(\beta v_2-V_{ref})+a_0\frac{di_{pm}}{dt} \end{aligned}. \tag{36}$$

We set $b_3\beta=a_3, b_2\beta=a_2+k_d, b_1\beta=k_p, b_0=k_i, a_0=k_c$ to simplify Eq. (36) as

$$s=k_d\frac{dv_2}{dt}+k_p(\beta v_2-V_{ref})+k_i\int(\beta v_2-V_{ref})+k_c\frac{di_{pm}}{dt}. \tag{37}$$

We assume that $b_3\beta=a_3$ does not affect the design freedom of the output response; the block diagram of the corresponding sliding mode controller based on the sliding mode surface (Eq. (37)) is shown in Fig. 6. In this diagram, i_{c0} is a feedback variable reflecting i_p; the feedback quantity achieves peak detection by the peak detector.

The selection of the sliding mode coefficient in the sliding mode controller is analyzed from the aspect of the system stability conditions.

Hypothesis:

$$v_{eq}=\frac{L_{eq}}{L_r}\frac{4}{\pi}v_{dc}\cos\beta-\frac{L_{eq}}{L_r}v_{crm}\cos(\beta-\gamma), \tag{38}$$

where

$$\begin{cases} \dfrac{di_{pm}}{dt}=\dfrac{1}{L_{eq}}\left(v_{eq}-\dfrac{4}{\pi}nv_2\right) \\ \dfrac{d^2i_{pm}}{dt^2}=\dfrac{1}{L_{eq}}\left(\dfrac{dv_{eq}}{dt}-\dfrac{4}{\pi}n\dfrac{dv_2}{dt}\right) \end{cases}. \tag{39}$$

Using Eqs. (31), (32), and (39), we obtain

$$n\frac{2}{\pi}\frac{dv_{eq}}{dt}=-k_d\frac{d^2v_2}{dt^2}-k_p\frac{dv_2}{dt}-k_i(\beta v_2-V_{ref})+n^2\frac{8}{\pi^2}\frac{dv_2}{dt}. \tag{40}$$

The output voltage expressed in Eq. (29) is calculated using the differential

$$\frac{d^2v_2}{dt^2}=\frac{1}{C_0}\left(n\frac{2}{\pi}\frac{di_{pm}}{dt}-\frac{1}{R_L}\frac{dv_2}{dt}\right). \tag{41}$$

We combine Eqs. (40) and (41) as follows:

$$n\frac{2}{\pi}\frac{dv_{eq}}{dt}=(n^2\frac{8}{\pi^2}-k_p+k_d\frac{1}{R_LC_0})\frac{dv_2}{dt} -k_d\frac{1}{C_0}n\frac{2}{\pi}\frac{di_{pm}}{dt}-k_i(\beta v_2-V_{ref}) \tag{42}$$

We substitute Eqs. (38) and (41) into Eq. (29) to obtain the input/output feedback linearization model of the subsystem.

$$\begin{cases}\dfrac{dv_{eq}}{dt}=\dfrac{\pi}{2n}\dfrac{1}{C_0}(n^2\dfrac{8}{\pi^2}-k_p+\dfrac{k_d}{R_LC_0})\left(\dfrac{2n}{\pi}i_{pm}-\dfrac{v_2}{R_L}\right) -\dfrac{\pi}{2n}k_i(\beta v_2-V_{ref})-\dfrac{k_d}{L_{eq}C_0}\left(v_{eq}-\dfrac{4}{\pi}nv_2\right)\\ \dfrac{di_{pm}}{dt}=\dfrac{1}{L_{eq}}\left(v_{eq}-\dfrac{4}{\pi}nv_2\right)\\ \dfrac{dv_2}{dt}=\dfrac{1}{C_0}\left(\dfrac{2n}{\pi}i_{pm}-\dfrac{v_2}{R_L}\right)\end{cases} \tag{43}$$

The linear subsystem variables (v_2 , v_{eq} , i_{pm}) are completely decoupled from the internal system ($i_{Lrm},\alpha,\beta,\gamma$) to enable the analysis of the system stability and the output voltage response on the basis of the linear subsystem using Eq. (43).

The state-space equation of the linear subsystem can be obtained by Eq. (43).

$$\begin{cases}\dot{x}=Ax+Bv\\ y=Cx+D\end{cases}, \tag{44}$$

where $x=[v_{eq},i_{pm},v_2],u=V_{ref},y=v_2$,

$$A=\begin{bmatrix}-k_d\dfrac{1}{L_{eq}C_0} & \dfrac{1}{C_0}(n^2\dfrac{8}{\pi^2}-k_p+k_d\dfrac{1}{R_LC_0}) & \dfrac{4}{\pi}n\dfrac{k_d}{L_{eq}C_0}-\dfrac{\pi}{2n}\dfrac{1}{R_LC_0}(n^2\dfrac{8}{\pi^2}-k_p+\dfrac{k_d}{R_LC_0})-\dfrac{\pi}{2n}k_i\beta\\ \dfrac{1}{L_{eq}} & 0 & -\dfrac{4}{\pi}n\dfrac{1}{L_{eq}}\\ 0 & \dfrac{2}{\pi}n\dfrac{1}{C_0} & -\dfrac{1}{R_LC_0}\end{bmatrix}$$

$$B=\begin{bmatrix}\dfrac{\pi}{2n}k_i\beta & 0 & 0\end{bmatrix}^T,C=\begin{bmatrix}0 & 0 & 1\end{bmatrix},D=0$$

The transfer function of the system is

$$H(s)=\frac{Rk_i}{L_{eq}C_0Rs^3+(L_{eq}+Rk_d)s^2+Rk_ps+Rk_i}. \tag{45}$$

The characteristic equation of the system is

$$L_{eq}C_0Rs^3+(L_{eq}+Rk_d)s^2+Rk_ps+Rk_i. \tag{46}$$

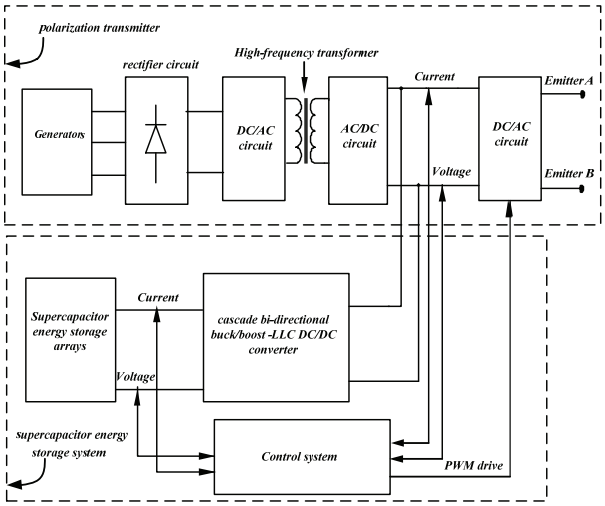

Fig. 9. Block diagram of the supercapacitor energy storage system.

IV. Experimental Verification

To test the feasibility of the theoretical research and the performance of the key technology of the supercapacitor energy storage system in the IP transmitter, we use the DSP TMS320LF2812 as the core of the system control. A laboratory test platform of the supercapacitor energy storage system is developed considering the energy storage requirement of the transmitter system of the polarization instrument. A block diagram and a specific structure diagram of the system are shown in Figs. 9 and 10, respectively. The system comprises the polarization instrument emission and supercapacitor energy storage systems. The polarimeter transmitter system consists of a three-phase power supply, the rectification circuit, a high-frequency inverter, the AC/DC circuit, and the DC/AC circuit. The three-phase power supply provides a 380 V voltage. After rectifying, inverting, lifting, and rectifying, a 1000 V DC bus voltage is obtained. Finally, the inverter is inverted again, and the signal is produced by the emitter. The supercapacitor comprises the supercapacitor energy storage array, the cascade bi-directional buck/boost-LLC DC/DC converter circuit, the system control circuit, and the protection circuit.

A. Determination of Experimental Parameters

1) Calculation of the Volume Value of the Supercapacitor

According to the performance index of the supercapacitor energy storage system, the maximum voltage of the supercapacitor group is approximately 400 V; therefore, a voltage value of 500 V is selected for the supercapacitor group. The HCAPC-120 F/2.7 V monomer type is used in the supercapacitor group for series and parallel connections, and we design the energy storage array using the energy constraint method. In consideration of the margin, the number of series branches is

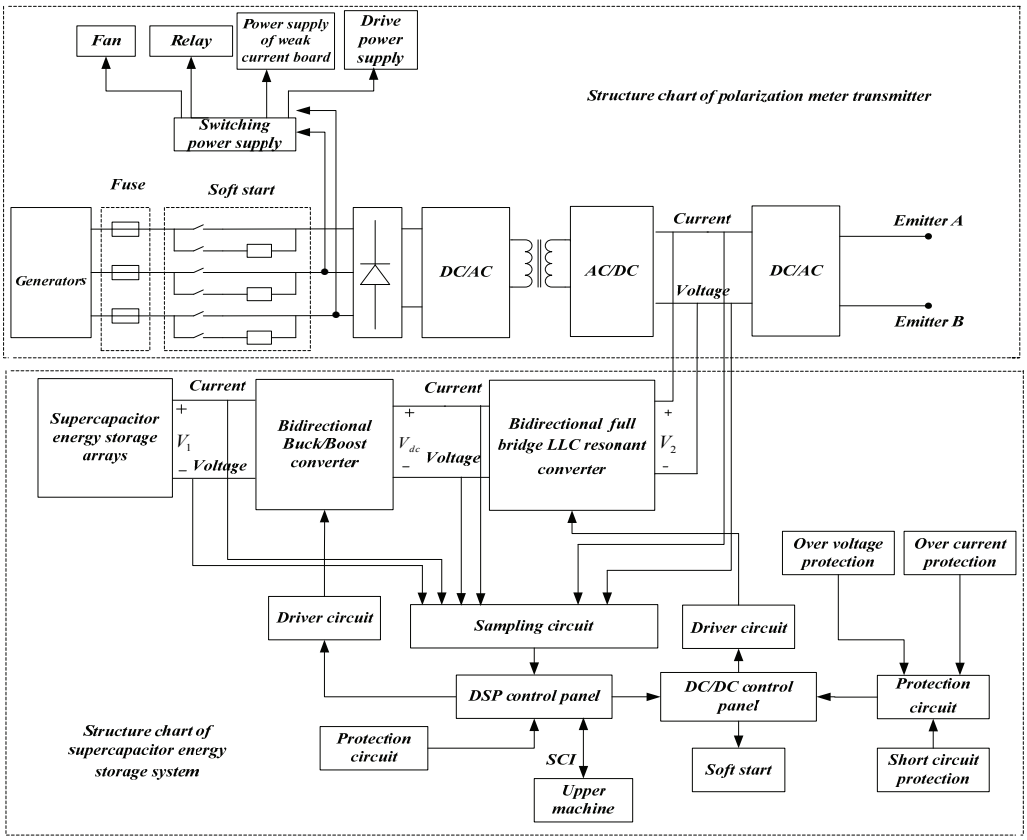

Fig. 10. Structure of the supercapacitor energy storage system.

TABLE I
DESIGN PARAMETERS OF THE MAIN POWER CIRCUIT FOR THE SUPERCAPACITOR ENERGY STORAGE SYSTEM

Parameter	Rating	Parameter	Rating
Supercapacitor voltage range（V_1）	200–400 V	Output voltage (V_2)	1000 V
One-stage converter output voltage（V_{dc}）	800 V	Rating output power（P_0）	10 kW
One-stage converter filter capacitance (C_{dc})	70 μF	Magnetic inductance (L_m)	992 μH
Resonant inductance (L_r)	198.4 μH	Resonant capacitance (C_{r1})	0.57 μF
Storage inductor (L)	300 μH	Resonant capacitance (C_{r2})	73.3 μF
Dead time	270 ns	Former vice edge of turns ratio	53:66
Two-stage converter filter capacitor (C_0)	2000 μF	Resonant frequency (f_s)	15 kHz
Discrete frequency ($f_{\min}$)	10 kHz	Discrete frequency ($f_{\max}$)	20 kHz

$m = \frac{V_{\max}}{V_F} = \frac{500}{2.5} = 200$ because $w_c = \frac{1}{2} C_{SC}(v_{sc1}^2 - v_{sc2}^2) \geq Pt$;

therefore, $\frac{120 \times n}{2 \times 200}(400^2 - 200^2) \geq 10000 \times 4$, $n \geq \frac{10000 \times 4 \times 2 \times 200}{120 \times (400^2 - 200^2)} = \frac{10}{9}$.

This means that the value of n is 2. That is, the supercapacitor energy storage array consists of 200 single capacitances in series and is connected in parallel with 2 layers. The final capacitor volume is 1.2 F, the voltage is 500 V, and the floating charge voltage is 540 V.

The output power of the energy storage system is 10 kW. The main parameters of the circuit are shown in Table I.

2) Sliding Mode Control Coefficient of Converter Operating in Boost Mode

The parameter analysis in boost mode shows that $\frac{\alpha_1}{\alpha_2} = \frac{10}{T_s} = 10000 s^{-1}$, $\frac{\alpha_3}{\alpha_2} = \frac{25}{T_s^2} = 25000000 s^{-2}$ using the reference voltage, $V_{ref} = 48V$, $\beta = \frac{V_{ref}}{V_{dc}} = 0.06 V/V$. Equations (11) and (12)

show that $K_3 = L\frac{\alpha_3}{\alpha_1} = L\frac{\alpha_3}{\alpha_2}\frac{\alpha_2}{\alpha_1} = 0.75$; by ensuring the system's stability and using the control parameters of the empirical method, $K = 119$ in Eq. (1) can be used to calculate $K_1 = 90, K_2 = 30.58$; therefore, the sliding mode control equation of the sliding mode controller is

$$\begin{cases} v_c = -18.35 i_{dc} + 5.4(48 - 0.06 v_{dc}) - 0.045 i_L + 0.06[v_{dc} - v_1] \\ \hat{} \\ vramp = 0.06 v_{dc} \end{cases} \quad (47)$$

3) Sliding Mode Control Coefficient of Converter Operating in Buck Mode

According to the requirements of the system, the sliding mode controller is designed for a critical damping response and the bandwidth is one-twentieth of the switching frequency f_S, namely, $f_{BW} = \frac{f_S}{20} = 0.75kHZ$, $\tau = \frac{1}{2\pi f_{BW}} = 200\mu s$; therefore, the adjustment time is $T_S = 5\tau = 1ms$ because $\frac{\alpha_1}{\alpha_2} = \frac{10}{T_s}$ and $\frac{\alpha_3}{\alpha_2} = \frac{25}{T_s^2}$ are known: $\frac{\alpha_1}{\alpha_2} = \frac{10}{T_s} = 10000 s^{-1}, \frac{\alpha_3}{\alpha_2} = \frac{25}{T_s^2} = 25000000 s^{-2}$. Using the reference voltage $V_{ref} = 48V$, $\beta = \frac{V_{ref}}{V_1} = 0.12V/V$ based on Eq. (23), with the known control parameters providing $K_{P1} = \beta L(\frac{\alpha_1}{\alpha_2} - \frac{1}{r_L C_1}) = 0.36Hs^{-1}$, $K_{P2} = LC_1\frac{\alpha_3}{\alpha_2} = 0.525V/V$. Therefore, the governing equations of the sliding mode controller are obtained on the basis of Eqs. (23) and (24).

$$\begin{cases} v_c = -0.36 i_{C1} + 0.525(48 - 0.12 v_1) + 0.12 v_1 \\ \hat{} \\ vramp = 0.12 v_{dc} \end{cases} \quad (48)$$

4) Calculation of Sliding Mode Control Parameters of the LLC Converter in Forward-Operation Mode

When a full-bridge bi-directional LLC DC/DC converter operates under a forward power flow, the equivalent output resistance under the rated power is $R_0 = \frac{V_2}{I_2} = \frac{1000}{10} = 100\Omega$, $L_{eq} = \frac{L_r L_m}{L_r + L_m} = 165.2\mu H$, and $C_0 = 2000\mu F$; using Eq. (46), we can obtain the transfer function

$$H(s) = \frac{100 k_i}{3.3\times10^{-5} s^3 + (1.65\times10^{-4} + 100 k_d)s^2 + 100 k_p s + 100 k_i}. \quad (49)$$

According to the root locus method and considering the dynamic response speed and the stability margin of the system, we can obtain

$$k_p = 0.95, k_i = 260, k_d = 9.835\times10^{-5}.$$

5) Calculation of Sliding Mode Control Parameters of the LLC Converter in Reverse Operation

When a full-bridge bi-directional LLC DC/DC converter operates under a reverse power flow, the equivalent output resistance under the rated power is $R_0 = \frac{V_{dc}}{I_1} = \frac{800}{12.5} = 64\Omega$, $L_{eq} = \frac{1}{n^2}\frac{L_r L_m}{L_r + L_m} = 258.05\mu H$, and $C_0 = 70\mu F$; using Eq. (46), we can obtain the transfer function

$$H(s) = \frac{64 k_i}{1.156\times10^{-6} s^3 + (2.58\times10^{-4} + 64 k_d)s^2 + 64 k_p s + 64 k_i}. \quad (50)$$

According to the root locus method and considering the dynamic response speed and the stability margin of the system, we can obtain

$$k_p = 0.86, k_i = 242, k_d = 1.52\times10^{-4}.$$

B. Experimental Test

The physical system is tested using an experimental platform for measuring the waveforms. The experimental platform is shown in Fig. 11.

Fig. 12 shows the bus bar voltage waveforms when the terminal voltage of the supercapacitor reaches a predetermined maximum value under the condition that the transmitter store energy system is charging. The experimental results show that the system is stable when both ends of the supercapacitor's voltage are $V_{sc} = 400V$, the one-stage DC bus voltage is $V_{dc} = 800V$, and the reverse input voltage is $V_2 = 1000V$. This finding indicates that the entire energy storage system operates normally when the power is in reverse flow.

When both ends of the supercapacitor's voltages reach the maximum value of 400 V, the enabling signal is given, and the energy storage system operates in power-forward mode. Currently, the supercapacitor discharges. Fig. 13 shows the voltage waveforms when the system is in a state of constant discharge. Evidently, the system stops discharging when V_{sc} is reduced to the minimum value of 200 V from the maximum value of 400 V; this process is maintained for 19 s. After the supercapacitor stops discharging, the voltage of the one-stage DC bus shows a linear decrease from the beginning, but the output voltage of the system (V_2) becomes stable after a short time. The system then operates normally under forward power flow. For a given voltage range, the supercapacitor continues to discharge for 19 s, and the storage system of the transmitter requires only 4 s to release the power; therefore, the supercapacitor guarantees the energy storage capacity of the system. The changes in waveforms V_{dc}, V_2 show that the system is capable of dynamic adjustment in forward- operating mode.

Fig. 11. System experiment platform.

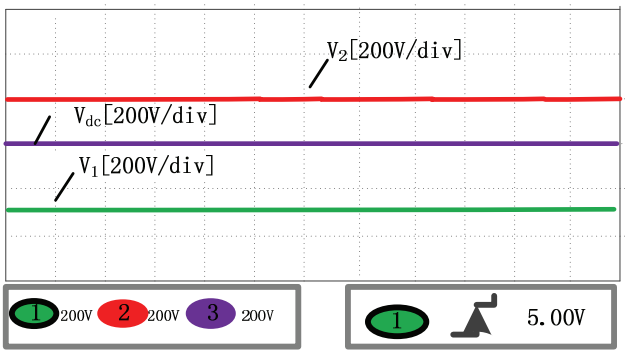

Fig. 12. Voltage waveforms after completed energy storage.

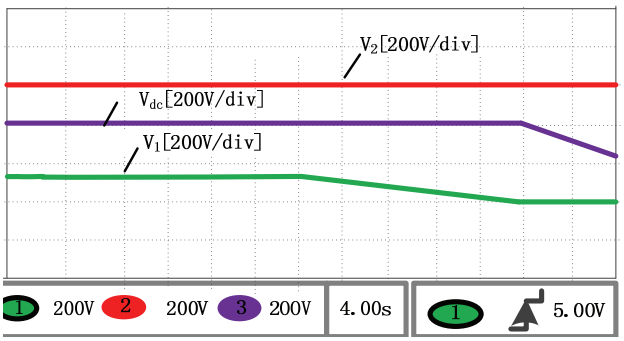

Fig. 13. Voltage waveforms when the system is in a state of constant discharge.

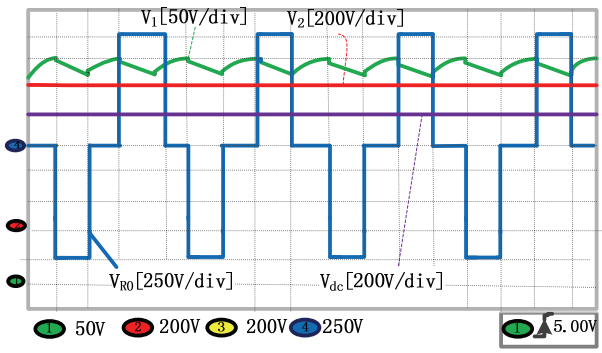

Fig. 14. Voltage waveforms when the system operates in a closed loop.

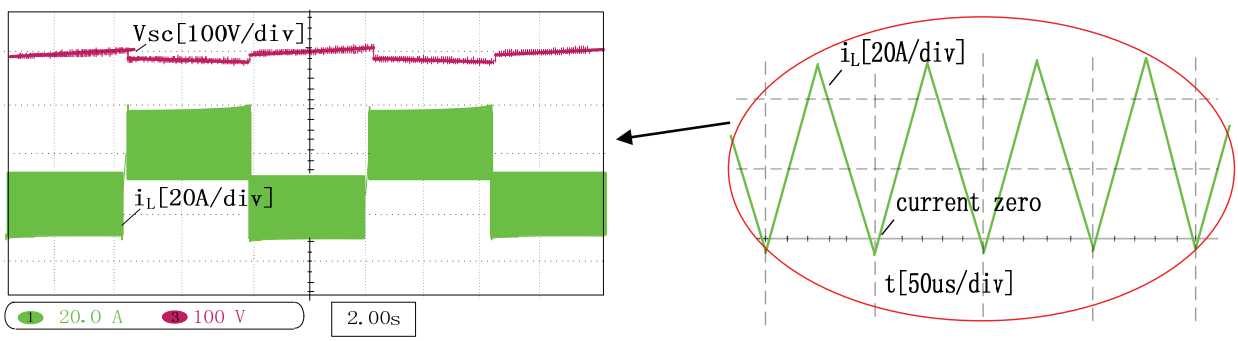

Fig. 15. Waveform of supercapacitor voltage and power inductor current when the output is stable.

The results of the experiment shown in Figs. 12 and 13 demonstrate that the topological structure of the system is correct; a two-way operating mode is achieved, and the system exhibits good performance and reliability.

Fig. 14 shows the voltage waveforms when the system operates in a closed loop. Evidently, when the IP instrument transmitter is working, the voltage at both ends of the supercapacitor is in a state of discharge, and the two-stage series converter is in the forward-operating state. When the transmitter does not work and has no load, the supercapacitor is charging, and the converter is in the reverse-operating state. During the switching process, under the bi-directional operating state, the DC bus voltage and the output voltage remain nearly unchanged. This situation demonstrates the stability and feasibility of the system and the superiority of the sliding mode control. V_{R0} in Fig. 14 is the external load voltage waveform of the transmitter.

Fig. 15 shows the waveform of the supercapacitor's charge–discharge voltage and power inductor current when the system output is stable. Apparently, for a given time of charge and discharge, the voltage range between the two ends of the supercapacitor is 360–400 V, which allows for constant power storage and release energy. In addition, the energy storage current waveform shows that the bi-directional buck/boost converter achieves zero-voltage switching (ZVS) when the current is over zero and the system achieves soft switching. Therefore, the proposed supercapacitor group satisfies the system's energy storage and release requirements.

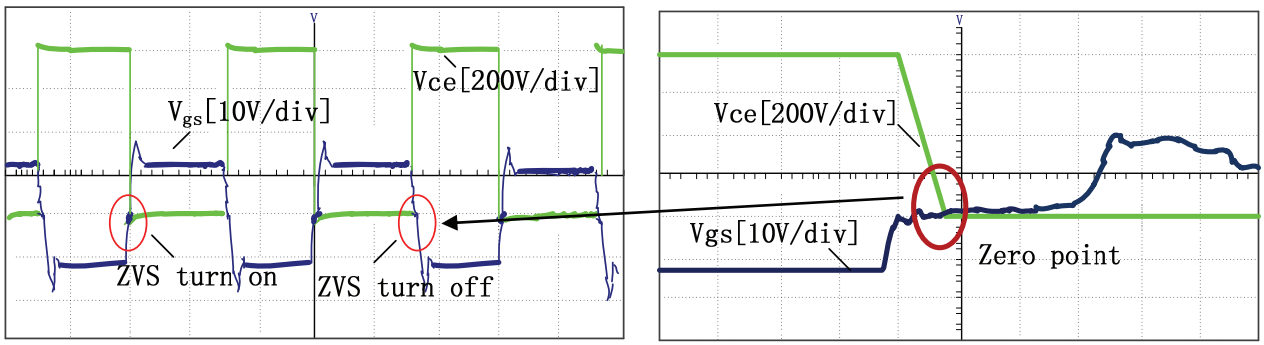

Fig. 16. Waveform of switch tube drive signal when the LLC converter operates in the forward state.

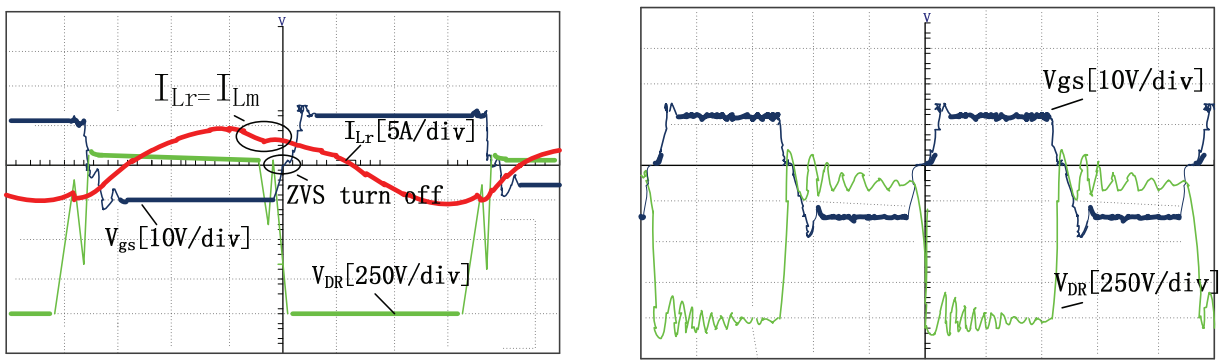

Fig. 17. Waveform of switch tube drive signal, rectifier diode voltage, and resonance current when LLC convertor work in forward state.

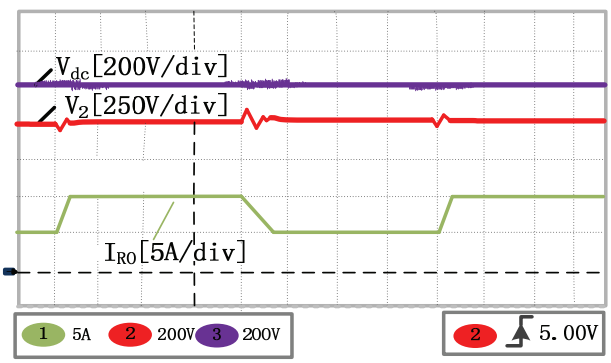

Fig. 18. Waveforms of the output voltage and output current under load mutation.

Fig. 16 shows the two-stage converter switch signal (Vgs) and the voltage (Vce) output voltage waveform at the two ends of the switch tube. As shown in Fig. 16, the switch tube achieves ZVS turn-on and turn-off, and the system achieves soft switching, thereby considerably reducing switching loss and improving system efficiency.

Fig. 17 shows the waveform of the switch tube drive signal, the rectifier diode voltage, and the resonance current when the LLC converter operates in forward state. When $i_{Lr} = i_{Lm}$, the ZVS turn-off of the rectifier diode is achieved in the proposed converter.

The results of the experiment shown in Figs. 15, 16, and 17 demonstrate that the main switch of the system achieves ZVS turn-on and turn-off and the rectifier two-stage tube achieves ZCS turn-off, thus substantially decreasing switching loss and enhancing system efficiency.

Fig. 18 shows the waveforms when the system power is flowing forward and the dynamic response exhibits load mutation. When the load is suddenly increased (from 200 Ω to 100 Ω), the dynamic adjustment time is 10 μs; the time is short and the system quickly and smoothly transitions to the operating state of the next load. When the load is suddenly reduced (from 100 to 200 Ω), the converter consumes approximately 75 μs to transition to the next steady-state operation. This situation occurs because the filter capacitance of the converter's forward output is larger; when the load decreases and the adjustment time of the state for the output filter capacitor is changed, the discharge time increases but the response speed of the sliding mode controller does not.

The results of a dynamic performance test of the full-bridge bi-directional LLC DC/DC converter are shown in Fig. 19. In this test, the converter operates in the forward- flow mode and the one-stage DC bus voltage mutates from 800 V to 700 V. Regardless of whether the input voltage is in a positive or negative transition, the output voltage has no transition process and the sliding mode controller immediately responds to enter the steady state. In the simulation of the system, the output voltage of the sliding mode controller is completely unaffected by the input voltage, but the experimental results show that the output voltage and output

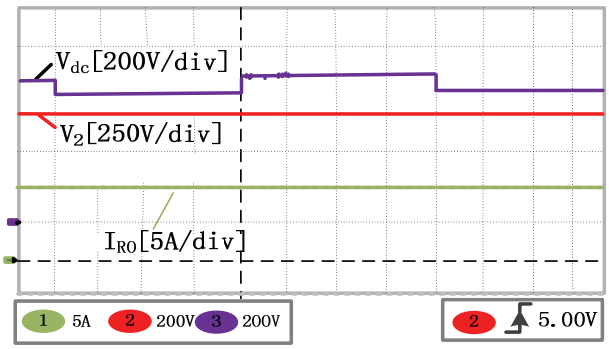

Fig. 19. Waveforms of the output voltage and current when the input voltage mutation occurs in the LLC converter.

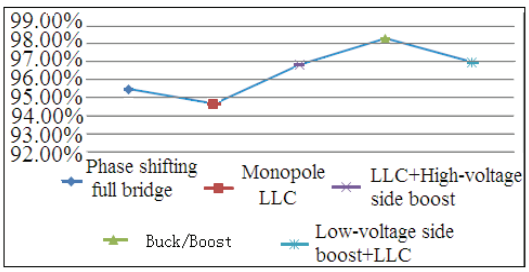

Fig. 20. Comparison of the efficiencies of different topologies.

current have different degrees of ripple changes due to the equivalent resistance of the filter capacitor, the current sampling resistance, and other factors.

The voltage waveform results shown in Figs. 18 and 19 indicate that the system has a fast, dynamic response and provides a stable and constant output under the condition of input voltage and load mutations. The system control method provides high reliability.

Fig. 20 shows the comparison of the total power loss using different topology converters under the same input and output voltage and output power of 10 kW.

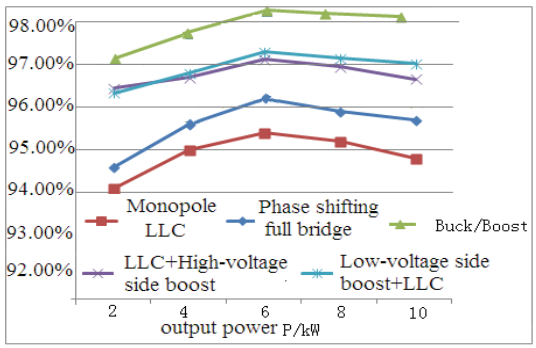

Fig. 21. Comparison of the bi-directional DC/DC converter efficiencies for five different topologies.

Fig. 21 shows a comparison of the efficiency of the supercapacitor energy storage system for different topologies under different power conditions.

Figs. 20 and 21 show that the efficiencies of the non-isolated buck/boost topology and the low-voltage side boost+LLC topology are higher than those of the other topologies. However, a single non-isolated buck/boost converter cannot be applied to high-power supercapacitor energy storage systems, which have a wide range of terminal voltage. Therefore, the low-voltage boost+LLC converter is the preferred topology for the energy storage system. A theoretical analysis and experimental tests are carried out.

In the experimental platform, the system is connected with a fixed resistance load of 100 ohms. The system performs efficiency tests on the rated input and output voltage (v_1 = 400 V, v_2 = 1000 V), different output powers, rated power, rated output voltage (p_0 = 10 kW, v_2 = 1000 V), and different input voltages. The test results are shown in Tables II and III.

The test results show that the system efficiency is approximately 97%, and the output stability of the system is stable.

TABLE II

EXPERIMENTAL DATA OF SYSTEM EFFICIENCY UNDER DIFFERENT OUTPUT POWER WHEN $V_1 = 400V, V_2 = 1000V$

System reference output power /kW	Actual input voltage /V	Energy storage inductance current /A	Actual output voltage /V	Actual output current /A	System efficiency /%
2	401	5.22	1006	2.01	96.46
4	400.5	10.39	1004	4.02	97.15
6	399.8	15.40	999.6	5.99	97.27
8	401.5	20.71	1005	8.04	97.17
10	402	25.9	1010	10.1	97.01

TABLE III

EXPERIMENTAL DATA OF SYSTEM EFFICIENCY UNDER DIFFERENT INPUT VOLTAGES WHEN $P_0 = 10kW, V_2 = 1000V$

System reference output voltage /V	Actual input voltage /V	Energy storage inductance current /A	Actual output voltage /V	Actual output current /A	System efficiency /%
200	205	51.31	1002	10.02	95.45
250	251	41.77	1005	10.05	96.34
300	298	34.59	997	9.97	96.44
350	352	20.97	1009	10.09	96.51
400	405	26.23	1015	10.15	96.97

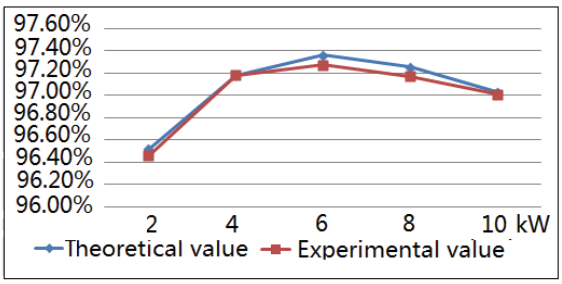

Fig. 22. Efficiency for different output power values when $V_1 = 400V, V_2 = 1000V$.

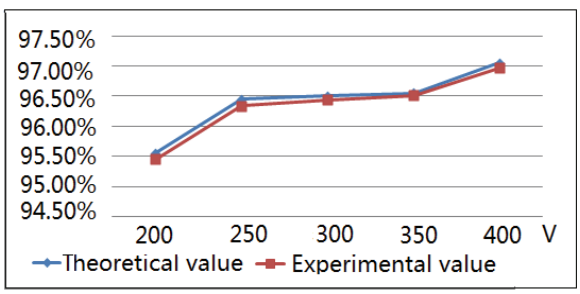

Fig. 23. Efficiency for different input voltages when $P_0 = 10kW, V_2 = 1000V$.

Figs. 22 and 23 show comparisons between the theoretical values and the measured values of the system efficiency under different output power values and different input voltages. The illustration shows that the experimental measurement is near the theoretical value.

V. Conclusions

In this study, the key technologies of a supercapacitor model, the power topological structure, and the control strategy of the energy storage system of an IP transmitter are designed and subsequently analyzed. In addition, an experimental system platform is developed. The experimental results validate the proposed bi-directional topology of the energy storage power system; the sliding mode control strategy with a variable structure is effective and superior. A soft switching technology is achieved for the system operation. The experimental calculation results show that the system's control accuracy remains stable at less than 2.5%, and the system efficiency is approximately 97%. The system can store and release energy on the basis of the requirements of the IP transmitter; therefore, the design of the supercapacitor energy storage system fully satisfies the requirements of the IP transmitter system in the excitation polarization instrument. The correctness of the theoretical analysis and the circuit design and the validity of the results are verified by the experimental results of the practical applications of the supercapacitor energy storage system.

Acknowledgment

This work was supported by the National Natural Science Foundation of China (61403127,61703144), Tackling Key Project of Henan Science and Technology (182102210051), Key Laboratory of Control Engineering of Henan Province (KG2016-01; Henan Polytechnic University China), Key Scientific Research Project of Henan Province (18B470005; Henan Polytechnic University China),Fundamental Research Funds for the Universities of Henan Province (18B470005) and Doctoral Fund of Henan Polytechnic University (B2017-23; Henan Polytechnic University China).

References

[1] S. Li，X. Kang, and K. M. Smedley, "Analysis and design of a family of two-level PWM plus phase-shift-modulated DC–DC converters," *IEEE Trans. Ind. Electron.*,Vol. 65, No. 6, pp. 4650-4660, Mar. 2018.

[2] R. Sathishkumar, K. K. Sathish, and K. M. Mahesh, "Dynamic energy management of micro grids using battery super capacitor combined storage" in *2012 Annual IEEE India Conference*, pp. 1078-1083, 2012.

[3] Y. Zhang, X. F. Cheng, C. Yin, and S. Cheng, "A soft-switching bidirectional DC-DC converter for the battery super-capacitor hybrid energy storage system," *IEEE Trans. Ind. Electron.*, Vol. 65, No. 10, pp. 7856-7865, May 2018.

[4] M. Pahlevaninezhad, J. Drobnik, P. K. Jain, and A. Bakhshai, "A load adaptive control approach for a zero-voltage-switching DC/DC converter used for electric vehicles," *IEEE Trans. Ind. Electron.*., Vol. 59, No. 2, pp. 920-933, Feb. 2011.

[5] J. Wang, B. Ji, H. Wang, N. Chen, and J. You, "An inherent zero-voltage and zero-current-switching full-bridge converter with no additional auxiliary circuits," *J. Power Electron.*, Vol. 15, No. 3, pp. 610-620, Mar. 2015.

[6] B. Zhao, Q. Song, W. Liu, and Y. Sun, "Overview of dual-active-bridge isolated bidirectional DC-DC converter for high frequency link power-conversion system," *IEEE Trans. Power Electron.*, Vol. 29, No. 8, pp. 4091-4106, Aug. 2014.

[7] D. Segaran, D. G. Holmes, and B. P. Mc Grath, "Enhanced load step response for a bidirectional DC-DC converter," *IEEE Trans. Power Electron.*, Vol. 28, No. 1, pp. 371-379, Jan. 2013.

[8] Y. Cai, H. Yin, J. Zhang, and X. Xia, "Discussion on working principle and application effect of polarization method," *Mineral Exploration*, Vol. 3, No. 2 pp. 212-217, Apr. 2012. (in Chinese)

[9] G. J. Wang, R. Wang, K. F. Shi, "The TDIP transmitter of energy storing with super-capacitors," *The 10th China International Geo-Electromagnetic Workshop*, pp. 136-138, 2011. (in Chinese)

[10] F. M. Ibanez, "Analyzing the need for a balancing system in supercapacitor energy storage systems," *IEEE Trans. Power Electron.*, Vol. 33 No. 3, pp. 2162-2171, Sep. 2017.

[11] S.-C. Tan, Y.-M. Lai, and C.-K. Tse, *Sliding Mode Control of Switching Power Converters: Techniques and Implementation*, CRC Press, 2011.

[12] P. Wang, C. D. Zhao, Y. P. Gao, Y. Zhang, and J. Li. "A bidirectional three-level DC-DC converter with a wide voltage conversion range for hybrid energy source electric vehicles," *J. Power Electron.*, Vol. 17, No. 2, pp. 334-345, Feb. 2017.

[13] J. Echeverria, S. Kouro, M Perez, and H Abu-Rub, "Multi-modular cascaded DC-DC converter for HVDC grid connection of large-scale photo-voltaic power systems," in *9th Annual Conference of the IEEE Industrial Electronics Society (IECON),* pp. 6999-7005, 2013.

[14] C. M. Lai, Y. H. Cheng, M. H. Hsieh, and Y. C. Lin, "Development of a bidirectional DC/DC converter with dual-battery energy storage for hybrid electric vehicle system," *IEEE Trans. Veh. Technol.*, Vol. 67, No. 2, pp. 1036-1052, Feb. 2018.

[15] Z. Fang, J. Wang, S. Duan, K. Liu, and T. Cai, "Control of an LLC resonant converter using load feedback linearization," *IEEE Trans. Power Electron.*, Vol. 33, No. 1, pp. 887-898, Jan. 2018.

[16] H. Hu, X. Fang, F. Chen, Z. J. Shen, and I. Batarseh, "A modified high-efficiency LLC converter with two transformers for wide input-voltage range applications," *IEEE Trans. Power Electron.*, Vol. 28, No. 4, pp. 1946-1960, Apr. 2013.

[17] J. Yamamoto, T. Zaitsu, S. Abe, and T. Ninomiya, "PFM and PWM Hybrid controlled LLC converter," in *2014 International Power Electronics Conference (IPEC-Hiroshima 2014 - ECCE ASIA)*, pp.177-182, 2014.

[18] H. Ma, Q. Liu, and J. Guo, "A sliding-mode control scheme for llc resonant DC/DC converter with fast transient response," *Conference of the IEEE Industrial Electronic*, Vol. 2, No. 1, pp. 162-167, 2012.

[19] D. B. W. Abeywardana, B. Hredzak, and V. G. Agelidis, "Single phase grid-connected lifepo4 battery super-capacitor hybrid energy storage system with interleaved boost inverter," *IEEE Trans. Power Electron.*, Vol. 30, No. 10, pp. 5591-5604, Oct. 2015.

[20] C. Buccella, C. Cecati, H Latafat, P Pepe, and K Razi. "Observer-based control of LLC DC/DC resonant converter using extended describing functions," *IEEE Trans. Power Electron.,* Vol. 30, No. 10, pp. 5881-5891, Oct. 2015.

[21] D. De, C. Klumpner, C. Patel, K. Ponggorn, M. Rashed, G. Asher, "Modeling and control of a multi-stage interleaved DC–DC converter with coupled inductors for super-capacitor energy storage system," *IET Power Electron.*, Vol. 6, No. 7, pp. 1360-1375, Aug. 2013.

[22] X. Wang, J. Gao, M. Chen, X. Wei, Y. Wei, and Z. Zeng, "Faulty line detection method based on optimized bistable system for distribution network," *IEEE Trans. Ind. Informat.*, Vol. 14, No. 4, pp. 1370-1381, Apr. 2018.

[23] O. Hegazy, J. Van Mierlo, and P. Lataire, "Analysis modeling and implementation of a multidevice interleaved DC/DC converter for fuel cell hybrid electric vehicles," *IEEE Trans. Power Electron.,* Vol. 27, No. 11, pp. 4445-4458, Nov. 2012.

Zhihui Zeng was born in Jiangxi, China, in 1978. He received his B.Sc. and M.Sc. in electrical engineering from Henan Polytechnic University, Jiaozuo, China, in 2002 and 2008, respectively, and his Ph.D. from Beijing University of Technology, Beijing, China, in 2016. He is Associate Professor at Henan Polytechnic University, Jiaozuo, China. His research interests include electronics technology in clean energy power fields and switching power supplies.

Xiaowei Wang was born in Henan, China, in 1983. He received his B.Sc. and M.Sc. in electrical engineering from Henan Polytechnic University, Jiaozuo, China, in 2006 and 2011, respectively. He is pursuing his Ph.D. at the School of Electrical Engineering, Xi'an Jiaotong University, Shaanxi, China, while a lecturer at Henan Polytechnic University, Jiaozuo, China. His main research interests include fault location, power system protection, and power signal processing.

Yanfang Wei was born in Henan, China, in 1982. He received his B.Sc. and M.Sc. in electrical engineering from Henan Polytechnic University, Jiaozuo, China, in 2006 and 2008, respectively, and his Ph.D. from Hohai University, Nanjing, China, in 2012. He is Associate Professor at Henan Polytechnic University, Jiaozuo, China. His current research interests include flexible DC transmission and power system analysis.

Zhiguo Hu was born in Henan, China, in 1977. He received his B.Sc. in electrical engineering from Zhengzhou University, Zhenzhou, China, in 2000 and his M.Sc in control theory and control engineering from Henan Polytechnic University, Jiaozuo, China, in 2006. He is Associate Professor at Henan Polytechnic University, Jiaozuo, China. His current reseach interests include power signal processing and power quality control.

Yangxiao Yu was born in Henan, China, in 1981. She received her B.A. in English from Henan Polytechnic University, Jiaozuo, China, in 2003 and her M.A. from Hena University, Kaifeng, China, in 2008. She is Lecturer at Henan Polytechnic University, Jiaozuo, China. Her current research interests include English linguistics and teaching.

Zhigang Zhang was born in Hebei, China, in 1976. He received his M.Sc. in computer science and technology from Henan Polytechnic University, Jiaozuo, China, in 2007. He is Lecturer at the School of Information Engineering in Jiaozuo University, Jiaozuo, China. His current research interests include power signal processing and machine learning.